Journal of Structural Geology 201 (2025) 105543

Contents lists available at ScienceDirect

Journal of Structural Geology

journal homepage: www.elsevier.com/locate/sg

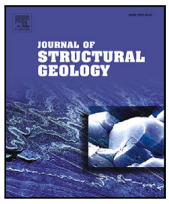

Graph-based fracture network analysis to integrate structural geology properties and identify preferential flow pathways in the aquifer system of Tsanfleuron, Swiss Alps

Ana Paula Burgoa Tanaka [a,b,*], Philippe Renard [a], Jefter Natan de Moraes Caldeira [c], Celia Trunz [a]

[a] Centre for Hydrogeology and Geothermics, University of Neuchâtel, Rue Emile-Argand 11, 2000, Neuchâtel, Switzerland
[b] Petrobras, Rua Marquês de Herval 90, 11010-310, Santos, São Paulo, Brazil
[c] Institute of Earth Science, University of Lausanne, Quartier Mouline, 1015, Lausanne, Switzerland

ARTICLE INFO

Keywords:
Graphs
Topology
Fractures
Betweenness centrality
Percolation
Karst

ABSTRACT

Graph theory has emerged as a promising method for analyzing fracture networks and complementing traditional geometrical descriptions. It emphasizes the network's topological aspects, highlighting the importance that fractures have in enhancing permeability and influencing flow anisotropy. However, integrating different structural geology analyses in a single framework remains a challenge. We propose a graph-based fracture network analysis combining geometry, topology, kinematics, age relationships, and geomechanics to identify the most important connections within a network. We apply it to the karstic aquifer system of Tsanfleuron, in the Western Helvetic Alps domain, where fractures play a crucial role in groundwater circulation and karstification. We acquired new structural data from a high-resolution digital elevation model (DEM), a 3D point cloud digital outcrop model (DOM), fieldwork, and one scanline. We interpreted and measured lineaments in 1:2.500 (DEM) and measured attitudes (DOM). Verification was done in the field, adding more measurements and the kinematics. The fracture network was transformed into a graph, and measurements were stored as attributes. Four main subvertical fracture sets were identified in chronological order, for the study site: E-W (85°), NE-SW (57°), N-S (176°), and NW-SE (117°). Censored fractures were identified to unbiased length, and abutting relationships were defined for pairs of sets to define age relationships. The E-W and NE-SW are the most persistent and longer fractures through all the site. The N-S set is localized in the central area, and the set NW-SE superimposes the others. The displacement is mostly dextral for the NE-SW and E-W faults, and sinistral for the N-S and NW-SE sets. Paleo tensor analysis results in NW-SE directed maximum compression. Fractures are opened and often enlarged by dissolution. Connectivity is moderate in terms of percolation. Betweenness and percolation centralities highlight the preferential water flow towards NE, ENE, and E.

1. Introduction

1.1. Fractures network as graphs

In structural geology, faults and fractures can be analyzed using a range of different complementary approaches described by Peacock et al. (2016), in terms of (i) geology, (ii) geometry, (iii) topology, (iv) kinematics, and (v) geomechanics. Peacock and Sanderson (2018) introduce additional elements such as age relationships, tectonics, and fluid flow, collectively referred to as the "seven pillars of wisdom" in structural geology. Structural analysis can be based on one or more pillars depending on the availability of the data and the type of problem to be solved.

The authors suggest that any structural study can be tailored to suit the desired outcome and that this scheme of analysis types should be used as a basis for the development of workflows, for the design of research projects, and to test hypotheses (Peacock and Sanderson, 2018). For example, the prediction of fluid flow through a fracture network must begin with a basic geological description of fracture types. Basic geological descriptions should be followed by measuring their geometries and topologies, understanding their age relationships, kinematics, geomechanics, and developing a realistic, data-led model

* Corresponding author at: Centre for Hydrogeology and Geothermics, University of Neuchâtel, Rue Emile-Argand 11, 2000, Neuchâtel, Switzerland.
E-mail address: ana.burgoa@unine.ch (A.P.B. Tanaka).

https://doi.org/10.1016/j.jsg.2025.105543
Received 25 June 2025; Received in revised form 26 August 2025; Accepted 27 August 2025
Available online 11 September 2025

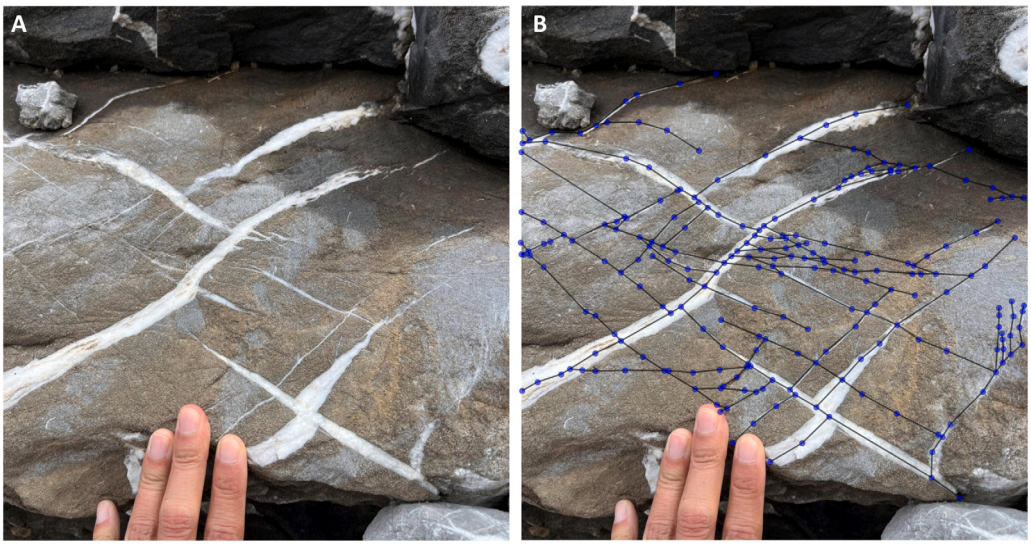

Fig. 1. Example of a fracture and vein network as graphs from an outcrop at Tsanfleuron. (A) fracture and vein network at the outcrop, (B) network as graphs, where nodes are intersections and edges are the branches of the structural features.

for related fluid flow. "Missing steps can lead to fundamentally flawed interpretations" (Peacock and Sanderson, 2018).

Graph-based fracture modeling has the potential to gather the different approaches and be designed to suit the "seven pillars of wisdom", as structural features and specifically fracture networks can be naturally thought of as graphs, where nodes represent fracture intersections and edges the fracture branches (Sanderson et al., 2019). In a 3D outcrop, each fracture can be associated with a node, and when two fractures cross, an edge is placed to represent the link between the two fractures (Andresen et al., 2013).

Fig. 1 is a schematic example of the 2D fracture and vein network as a graph; the graph was built based on the interpretation of an outcrop at the study site.

Graphs are well suited to the study of fracture networks, not only because they are considered complex systems, in relation to their fractal nature (Valentini et al., 2007), but also because this inherited complexity can be represented in an accessible form, thus broadening the range of analyses linked to graph theory.

Thiele et al. (2016) suggests the use of graph theory based methods as an efficient way to compare topological expressions in stratigraphy and structural geology. With graphs, it is possible to analyze the topology of the networks and "move beyond simple description of geometric parameters" (Sanderson et al., 2019). Topology describes the relationship between fractures and/or fracture sets, as an abstraction of its spatial relationships. As topology is invariant to scale and continuous changes, the approach allows for modeling topologies based on the recurrent ones found in real fracture networks.

Nyberg et al. (2018) and Casiraghi et al. (2025) use topology to define cross-cutting and abutting relationships, and to unbiased length distributions considering censoring sampling problems (Bonnet et al., 2001), as long fractures might intersect the boundary of the interpretation, or may not be identified as a single continuous structure due to weathering or deposit coverage (Casiraghi et al., 2025).

Nyberg et al. (2018) proposes a workflow with a set of tools available for geometrical and topological analysis of fracture networks in GIS. The toolbox is useful for all stages of fracture characterization, from interpretation to flow. Benedetti et al. (2024) and Casiraghi et al. (2025) also propose tools for the characterization of fracture networks from digital outcrop models, tools are available in Matlab and Python. Both groups propose tools for fracture characterization, the first emphasizes the use of graphs and in a structured workflow, and the second focus in separate applications for virtual outcrops, such as estimating length distributions, considering censoring.

Together with fracture geometry (orientation, density, and length), topology plays an important role in the connectivity of natural fractured systems, as described by Manzocchi (2002) and Sanderson and Nixon (2015, 2018). The key issue is that standard stochastic fracture models are generally unable to represent a coherent topology of real fracture networks and, therefore, cannot represent conductivities similar to natural fracture networks (Manzocchi, 2002; Sanderson and Nixon, 2018), resulting in different flow properties (Sanderson and Nixon, 2015) and Sævik and Nixon (2017).

With the application of graph theory and tools, it is possible to evaluate connectivity using two concepts described by Sanderson and Nixon (2018): (i) a measure of elements that are interconnected, in terms of degrees or centralities, and as (ii) a threshold above which the network is connected, in terms of percolation. In (i) the degrees of each node and its centralities are computed, and the highest degrees describe the most connected intersections of the fracture network (Santiago et al., 2016). In (ii) bond percolation (Aharony and Stauffer, 2003) can be calculated from the graph network by progressively removing nodes and tracking the size of the largest connected components of the fracture network.

1.2. Objectives

The objective of the paper is to demonstrate how to use graph theory for the analysis of fracture networks in a case study in the Swiss Alps. Our aim is to define the most important nodes in the fracture network and to identify potential preferential flow paths. The graph gathers all available data from different acquisitions and approaches that can be rapidly accessed to characterize geometries (azimuths, length, aperture), topology (degrees and centralities), and kinematics (normal, reverse, dextral, sinistral) as attributes from nodes and edges. This approach avoids gridding and meshing, or the selection of a sampling area, in the early stages of fracture characterization and modeling, differentiating it from previous approaches.

To illustrate the approach, we applied it to the Tsanfleuron site, where new data have been acquired and are presented in this paper. The results will later be used to constrain a hydrogeological model of the area. Therefore, a second aim of the paper is to present this novel description of the fracture networks in the Tsanfleuron area.

1.3. Study site and geological context

Located in the western domain of the Helvetic Alps, in the Diablerets Massif, the glacierized karst aquifer system of Tsanfleuron (Fig. 2), Switzerland, is a key study site to understand the links between geological structures and groundwater circulation in the Alps.

The upper part of the aquifer is recharged by precipitation and by the overlying and rapidly retreating glacier. The aquifer is drained at its lowest point by the Glarey spring (Fig. 2C, D) (Gremaud et al., 2009). The retreating glacier exposed the fractured pavement, where fractures of different ages influence the circulation of underground water and are related to the karstification of the limestone aquifer (Schoeneich and Reynard, 2021; Gremaud et al., 2009; Franck et al., 1984). The main karstified formations are the Cretaceous limestones (Urgonian facies) in the upper part of the lapiaz and Eocene limestones in the lower part, separated by a stratigraphic gap that is a product of the uplift and regression starting in the Palaeogene (Schoeneich and Reynard, 2021; Gremaud et al., 2009) (Fig. 2E).

The geology, geometry, kinematics, ages relationships, tectonics, and influence of structural geology on the development of karst have been described for the region that includes Tsanfleuron by Franck et al. (1984), Schoeneich and Reynard (2021), and specifically for Tsanfleuron by Gremaud (2008) and Gremaud et al. (2009).

Schoeneich and Reynard (2021) describe the structures and tectonic evolution of the Diablerets Massif tectonically as part of the Helvetic Alps, formed by the Helvetic nappes of Morcles, and Wildhorn, the last subdivided into the Diablerets, Mt Gond, and Sublage nappes (Escher et al., 1993; Epard, 2001; Steck et al., 1997) (Fig. 2B). The glacio-karstic area of Tsanfleuron is a 10 km^2 karstified area developed on limestones from the back of the Diablerets nappe (Fig. 2C), and in part of the overlying Mont-Gond nappe (Gremaud et al., 2009). An isoclinal syncline connects the two nappes and plays an important role in the circulation of underground water in the area, the Diablerets nappe is gently folded, forming a huge anticlinorium, its axis plunges 5° to 10° to ENE (Gremaud et al., 2009; Steck et al., 2001; Schoeneich and Reynard, 2021).

The tectonic evolution of the constraints of the Col du Sanetcsh, the region that comprises the Tsanfleuron lapiaz, is described by Franck et al. (1984) who studied the brittle tectonics and seismicity of the region. In terms of geometry and age relations, the authors describe three fault systems, chronologically ordered as: NE-SW (60°–70°), N-S (180°), and NW-SE (130°–150°).

Gremaud (2008) and Gremaud et al. (2009) add a fourth set of fractures to the previously described systems, chronologically ordered as: E-W (90°), NE-SW (60°), N-S (0°), and NW-SE (135–145°). The added E-W set is described as local but important at this scale. The development of paleokarst was influenced by the oldest alignments that were active before and during the deposition of the Eocene sediments; it was stopped by the marine transgression and by the thrust of the overlying nappes (Gremaud, 2008; Gremaud et al., 2009).

2. Methodology

Faults, joints, and veins are designated as general fractures in the present work, the structures are specified throughout the text when necessary. Fracture measurements and the analyses used in this work are available in Python, as data files, and jupyter notebook examples, in a github repository[1] (Tanaka, 2025).

[1] https://github.com/anapaulabtanaka/tsanfleuron_fracture_networks

2.1. Fracture interpretation and measurements

A total of 3340 fractures were interpreted and measured using different acquisition methods: 2D fracture interpretation using a digital elevation model (DEM) and photo orthomosaic ($N = 2915$), 3D fracture interpretation using a 3D point cloud as digital outcrops (DOM) ($N = 48$), field measurement ($N = 192$), and a scanline acquisition ($N = 185$) (Fig. 3).

To analyze all directional data statistics, we plot azimuths using rose diagrams with Python, because of the 2D nature of the measurements done using the DEM. The number of bins was calculated according to the number of samples available, using Rice's rule: The number of bins is the cube root of the number of observations times two. The selection of bins according to sample size, the use of equal-area wedges to plot the rose diagrams, and the set definition follow suggestions from Sanderson and Peacock (2020).

For other types of acquisition, when dips are available, we use stereograms generated with openstereo (Grohmann and Campanha, 2010). The definition of family sets is done with the definition of slopes from a fractional cumulative frequency curve of the sorted azimuths, five slopes were identified, and the breaking points were approximate to azimuths that define the azimuth ranges of the fracture sets as: N-S (0°–40° and 140°–180°), NE-SW (40°–70°), E-W (70°–100°), and NW-SE (100–140°).

2.1.1. Digital models (DEM and DOM)

A digital elevation model (DEM) and an orthomosaic photo (Fig. 4A) were the basis for the 2D interpretation of fracture lineaments, the DEM and photos were the products of several UAV flights that were taken above the Tsanfleuron Glacier in 2019 with a Sense Fly EBEE UAV, at altitudes between 300 and 600 m above ground, and a resolution of 10 cm/px resolution. The acquisition and processing of UAV data was done for a study of the glacier thickness described by Neven et al. (2021).

The DEM was first used for the reconnaissance of the study site in terms of fracture patterns. The initial approach considered different scales, like 1:15.000 to picture the whole study site, then 1:5.000 to zoom in on specific areas and verify the structures in more detail, and then later in 1:2.500, which was the final scale set to interpret the fracture networks. A total of 2915 fracture segments were interpreted in 2D (Fig. 3).

The interpretation was done using QGIS, the branches are mapped as lines (linestrings) and snapping was done at all intersections to maintain the topology of the network. The length and azimuth measurements were calculated from the geometries of the interpreted fractures. The mean fracture density (P21) (Dershowitz and Herda, 1992) was calculated for the whole study site by sets, with a grid cell size of 40 × 20m; the values are relative and can be recalculated according to different sampling areas.

The 60% overlap of 130 orthophotos allowed the generation of a 3D point cloud with photogrammetry (Fig. 3), the high-precision DEM (swissALTI3D, from swissTopo) was used as a basis for orthorectification. A total of 48 points were identified and measured in terms of fault length, attitude, and kinematics, using Cloud Compare. 3D fault identification is possible on virtual outcrops due to fault displacement.

2.1.2. Field work and scanline

We verified the structures that were interpreted and measured in 2D and 3D by comparing some measurements in the field to check if they correspond to fracture surfaces and their attitudes. An interpretation pitfall could be to mistake a glacier striae by a fracture lineament in the 2D interpretation.

We also measured in the field 192 fractures (faults and joints), 53 lineations (striae and slickenside), 3 stilolytes, 1 fold axis, and 7 beddings. The attitudes were measured using a Clar compass, and a digital compass-clinometer from the application FieldMove Clino (Petroleum

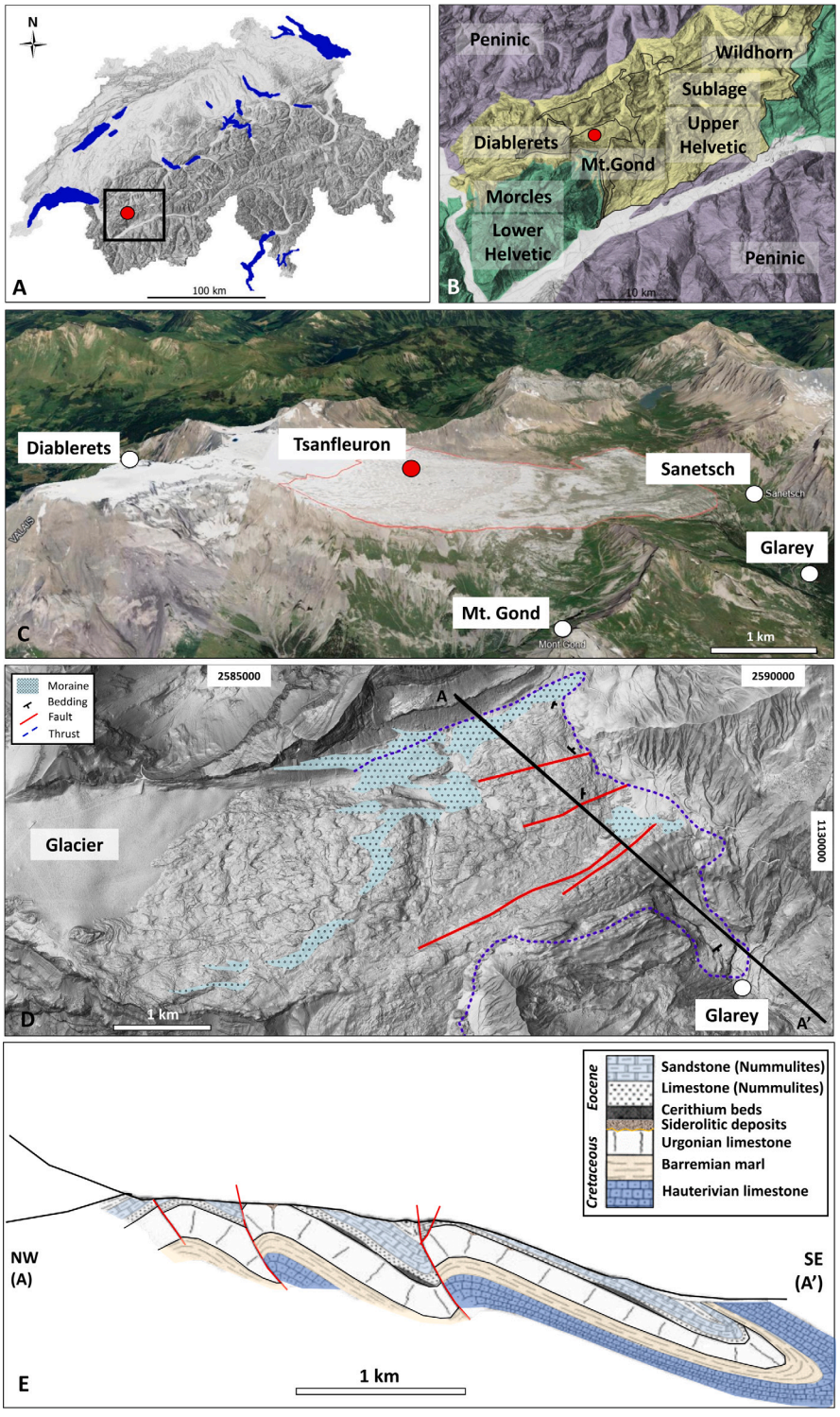

Fig. 2. Location of Tsanfleuron in the Western Swiss Alps (red dot). (A) Base map of Switzerland (DEM swissALTI3D, swisstopo). (B) Position at the Upper Helvetic (modified from the tectonic map of Switzerland, 1:500.000). (C) 3D view of Tsanfleuron and surroundings (Google Earth: Google, Airbus, Landsat/Copernicus, Data SIO, NOAA, U.S. Navy, NGA, GEBCOGeoBasis, imagery from 8/1/2012–newer). (D) Pavement zoom in 2D (DEM SwissALTI3D, swisstopo) highlighting physiographic features and tectonic elements (modified from the geocover, swisstopo, and Gremaud, 2008). (E) NW-SE (A-A') cross section, simplified from Badoux et al. (1959) (geological atlas of Switzerland 1:25000). (For interpretation of the references to color in this figure legend, the reader is referred to the web version of this article.)

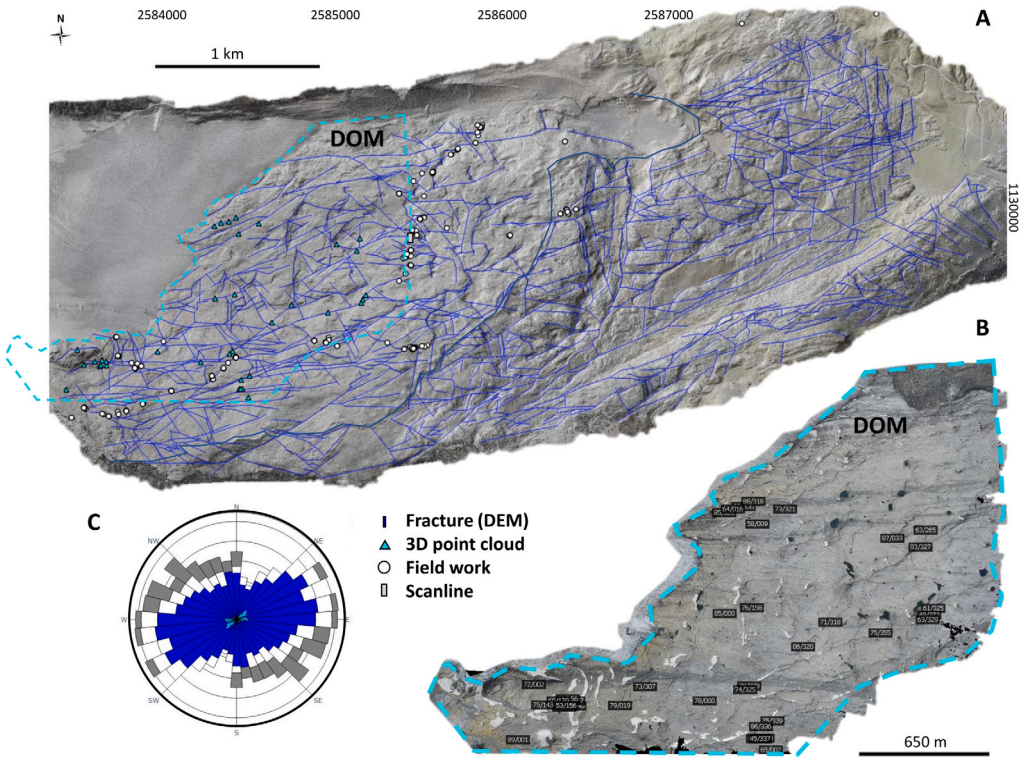

Fig. 3. All structural measures and interpretation from different sources. (A) Fracture interpretation from the DEM (blue), field (white dots), scanline (gray box), and from the 3D point cloud (cyan triangles), the DOM is highlighted in dashed cyan. (B) Measurements in the point cloud (black labels in the DOM). (C) Rose diagram of equal area of all the azimuth measurements acquired by data source. (For interpretation of the references to color in this figure legend, the reader is referred to the web version of this article.)

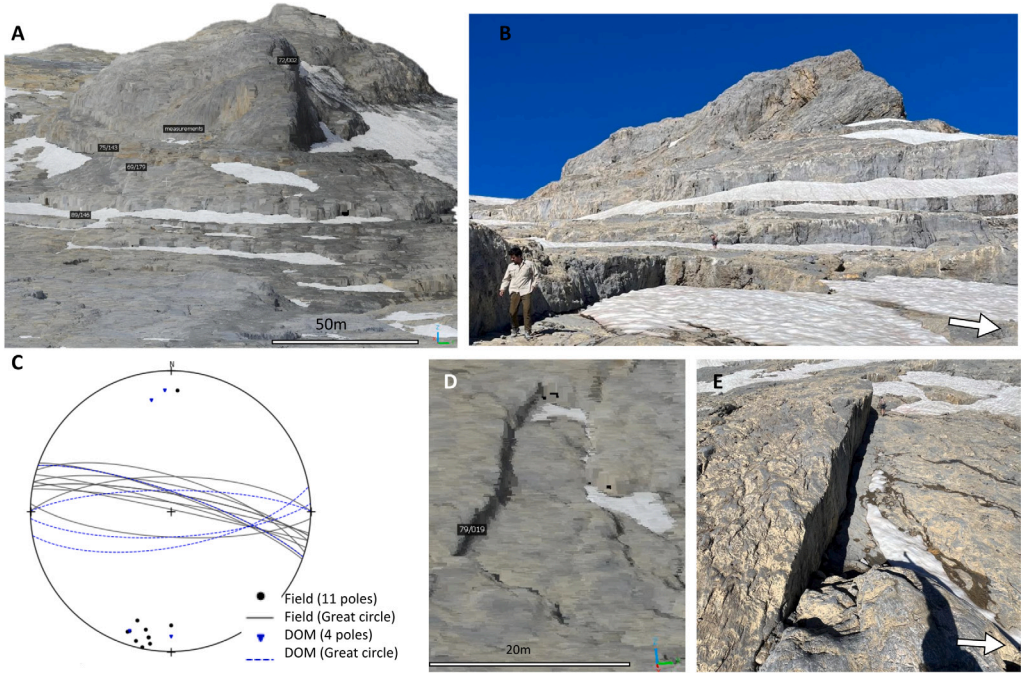

Fig. 4. Measurements done using DOM and/or at the field. (A) Inaccessible points from the 3D point cloud. (B) Inaccessible points at the field. (C) Stereogram with the comparison between measurements from the DOM (blue triangles and dashed great circles) and from the field (black poles and black great circles) of a E-W fault. (D) E-W fault measured from the DOM. (E) E-W fault measured from the fieldwork. (For interpretation of the references to color in this figure legend, the reader is referred to the web version of this article.)

Experts Limited), with a declination of 3.16°. Kinematic analysis and paleostress tensor inversion are performed using WinTENSOR (Delvaux and Sperner, 2003), back tilting was performed for the analysis of older fracture sets (assuming that they were formed before nappe imbrication).

We acquired 20 m of a scanline planned to sample a NW-SE fracture corridor, measuring additional 185 fractures. With the scanline, we added more samples to the NW-SE set, and 38 aperture measurements that were measured using a meter rule. The scanline methodology is done using panoramic photos registered with a tablet to aid in data acquisition and processing.

2.2. Graph-based fracture modeling

2.2.1. Fracture network as graphs

We transform the fracture network into a graph, using an algorithm that we designed based on the Python package NetworkX,[2] where the nodes correspond to the fracture intersections and the edges represent branches (Fig. 1). The modeling workflow starts by reading the fracture interpretation as a data frame, fracture linestrings are transformed into graphs by iterating through the data frame and extracting the coordinates of the intersections to add nodes and edges to a new graph. The coordinates are stored as a position attribute for each index of the nodes.

The lengths of segments and angles are calculated directly from the graph, using the distance between the extremities of the edges for length and calculating the tangent arc for the azimuth. The unbiased length is calculated with the correction of the censored area by applying a non-parametric Kaplan–Meier estimator of the empirical survival function and unbiasing with a maximum likelihood estimator (MLE), as proposed by Benedetti et al. (2024) and Casiraghi et al. (2025), using the Python package Fracability.[3]

The selection of the best statistical model that describes the length distribution is done by calculating the distances from the empirical distribution to the statistical models. Estimation of scaling parameters is done using maximum likelihood (MLE) (Rizzo et al., 2017; Casiraghi et al., 2025) as a more accurate statistical approach to increase the reliability of fracture data analysis, than the common inference that relies on the calculation of the slope of a regression line. We compare power law, exponential, gamma, and lognormal models as they are the most commonly used for fracture network analysis (Bonnet et al., 2001), to select the best fit, we use several criteria, Akaike, Kolmogorov–Smirnov, Koizol and Green and Anderson–Darling estimations to calculate the distances, as proposed by Benedetti et al. (2024) and Casiraghi et al. (2025).

Geometry, topology, kinematics, and geomechanics measurements are stored as attributes in the nodes and edges. Measurements that could not be acquired for all the fractures were generalized in the graph by sets, for example mean dip, type of displacement, and relative aperture, resulting in a basic node structure like: (node index, position (x,y), family, length, azimuth, radians, mean dip, kinematics, mean aperture, degree, betweenness, and percolation centrality). Other statistics, like minimum, maximum values, and standard deviation, can be calculated from the properties when needed or added as attributes.

2.2.2. Degrees and topological relations

For the topological analysis, the degrees of the nodes are calculated and stored as attributes. The degree of a node corresponds to the number of edges that are incident to the node. We refer to the type of node according to their degrees by numbers 1 to 5, which are equivalent to the nomenclature used to represent connectivity and fracture intersections combinations (Manzocchi, 2002; Sanderson and Nixon, 2015) as isolated fracture tips (I-nodes, degree 1), abutments or splays (Y-nodes, degree 3), and fracture intersections or crossings (X-nodes, degree 4).

Degree 2 nodes are removed from the network when analyzing the topology, as they are largely dependent on the type of interpretation and sampling criteria defined by the structural geologist. We use karstnet,[4] a Python package that provides tools for the statistical analysis of karstic networks to generate a simplified reduced graph, without nodes of degree 2, maintaining only junctions and extremities as seed nodes, which are later linked by an edge of unit length calculated from the explored path (Collon et al., 2017).

The proportion of nodes of degree three is calculated to identify abutting relationships as described by Sanderson et al. (2024) and Casiraghi et al. (2025) to obtain information about age relationships. The analysis is done with pairs of fracture sets, we count the number of node's degree 3 that abut each set. The higher number of abutting nodes defines the younger set from the pair.

2.2.3. Betweenness and percolation centrality

To evaluate preferential pathways, we calculate centralities to highlight the most important nodes of the network, using as a base, the functions from the Python package Networkx (Hagberg et al., 2008). Betweenness centrality (BC) is one of the most prominent measures of centrality (Brandes, 2008), it is defined in terms of the degree to which a point falls on the shortest path between others and therefore has the potential to control communication (Freeman, 1977). Quantifies the number of times a node acts as a connection in the shortest path between two other nodes, it is calculated by summing up the fractions of shortest paths between other pairs of nodes that pass through a node (Brandes, 2008) as:

$$BC(v) = \sum_{s,t \in V} \frac{\sigma(s,t|v)}{\sigma(s,t)} \tag{1}$$

Where v: node, V: set of nodes, $\sigma(s,t)$: number of shortest (s,t) paths, $\sigma(s,t|v)$: number of paths passing through some node v other than s,t.

Betweenness centrality measures the importance of a single node in a network in terms of pure topology, independently of changes in the node's state. Therefore, if there is percolation, the centrality measures are not adequate, for example, for infection transmission (Piraveenan et al., 2013). To quantify the percolation states of the nodes and the impact on their topological connectivity, Piraveenan et al. (2013) propose the measure of percolation centrality (PC). They define the percolation centrality for a node, as the proportion of 'percolated paths' that go through that node in a given time. The 'percolated path' is the shortest path between a pair of nodes, where the source node is percolated. The percolation centrality of node v in time t is:

$$PC^t(v) = \frac{1}{N-2} \sum_{s \neq v \neq r} \frac{\sigma(s,r|v)}{\sigma(s,r)} \frac{x_s^t}{[\sum x_i^t] - x_v^t} \tag{2}$$

Where i: percolation state of the node at time t, $x_i^t = 0$ indicates a nonpercolated state at time t, $x_i^t = 1$ indicates a fully percolated state at time t. The percolation centrality is equivalent to betweenness centrality when all nodes have the same percolated state, as shown in (1) and (2).

For both centrality calculations, the edges are weighted according to the segment length and used to calculate the weighted shortest paths, interpreted as distances.

To evaluate network connectivity, we simulate bond percolation (Aharony and Stauffer, 2003) in a modified way, directly from the graph network, progressively removing nodes randomly from the network and calculating the size of the largest connected components at each step. A threshold can be defined by plotting the fraction of nodes removed by the size of the largest connected component.

[2] https://github.com/networkx/networkx

[3] https://github.com/gecos-lab/FracAbility

[4] https://github.com/karstnet/karstnet

Table 1
Overall statistics by fracture set.

Set	Sample	Mean Az. [°]	Std. Az. [°]	Mode Az. [°]	Mean Dip [°]	Mean Length [m]	Mean Aperture [cm]	Mean P21 [m^{-1}]
E-W	965	85	8	89	73	222	0.167	0.016
NE-SW	695	57	8	63	75	248	0.400	0.024
N-S	897	176	24	160	75	147	0.220	0.006
NW-SE	783	117	12	130	81	151	0.443	0.006

3. Results

3.1. Structures verification in the field

Remote sensing and virtual outcrops are very useful, not only for the reconnaissance of the study site and the planning of field work, but also for the interpretation of fracture networks and the measurement of geometries such as length and orientation. The main positive aspect is the ability to virtually access outcrops that are physically difficult to reach, for example, areas with higher relief surrounded by snow in the west part of Tsanfleuron (Fig. 4A, B).

A subset of remotely interpreted fracture measurements was verified in the field using direct compass-based measurements (Fig. 4C). One of the possible pitfalls is to mistake fault-related lineations with striae from glacial advance and retreat; striaes are not described in this work, but can also be identified through remote sensing. In the field, the striae leave a smoother lineation than slickensides and as they describe the movement of the glacier over the rock, the sense of movement is the same in the two adjacent wall surfaces of the striae, differing from the slickenside that records opposite sense of movement in the footwall and hanging wall. Fractures are also more pervasive structures due to the nature of the displacement (faults), dissolution, or filling (veins), which is more evident in the DEM.

Another positive aspect of virtual outcrops is the faster measurements of fracture attitudes and length, to validate the attitude measurements (dip and dip azimuth) we compared them to the ones done in the field. The aim was not to do a detailed study about accuracy, but to compare if the measurements from DOM result in a similar orientation of the structures measured in the field and therefore if they are trustworthy to be added to the whole dataset. Fig. 4C illustrates the comparison between the measurements of the subvertical E-W fault in the field (Fig. 4E), and from the DOM (Fig. 4D). This indicates that the measurements done with the DOM are similar to the ones done on the field.

In the field, it was possible to verify the geometry of the N-S faults, since they are located in the central area of the study site, sometimes in a lower relief, generating steps that divide the area into east and west, where the lower parts in the east are greener due to the development of vegetation (Fig. 5A). At first glance, the N-S structures seemed to be related to the lower relief, and because they are clustered at the central part of the study site, they could be interpreted as a less important set for the generation of preferential pathways, while in the field we are able to observe an important fracture corridors of N-S fractures associated with the larger N-S faults.

Relay ramps (Fig. 5B), the subvertical dips of fractures (Fig. 5B, C, D), and dissolution associated with fracture surfaces (Fig. 5A, B, C, D) are also more evident to analyze in the fieldwork. Lineation (Fig. 6A) and stylolite can only be measured in the field. Characteristics of a fracture filling can only be observed in the field (Fig. 5B). Kinematics interpretations based on rhombohedral and en echelon structures (Fig. 6C, D) associated with the degree of dissolution are only possible by field observations.

The bedding was also measured in the field to describe the gentle dip of the strata to ENE, E, and ESE with a mean attitude of 71/12 and a fold axis plunging towards E with an attitude of 92/12. The bedding measurement was not done next to the fold closures and close to the nappe front. An extensive bedding measurement was not carried out, as it was not the objective of the study.

3.2. Fracture network characterization

We transform the network of fractures into a graph, where the nodes correspond to fracture intersections and the edges represent branches (Fig. 7), then we calculate the geometric properties from the edges and store the information to the nodes, from the nodes we calculated degrees and centralities to identify the most important nodes. The complete Tsanfleuron graph has 2785 nodes and 2914 edges (Fig. 7), while the simplified graph has 1667 nodes and 1796 edges. The network has 125 connected components and 254 cycles.

3.2.1. Orientation, length, density, and aperture

Four main fracture sets were identified, with mean azimuths: E-W (85°), NE-SW (57°), N-S (176°), and NW-SE (117°) (Fig. 7). Fractures from set NE-SW and E-W (Fig. 5B, C) occur more frequently and are the most persistent throughout the site, the N-S set occurs locally in the central part of the area (Fig. 5A), and the set NW-SE superimposes the other sets but in a discontinuous way in terms of length, being less evident on the DEM in the 1:2.500 scale but more evident in the field (Fig. 5D).

The general statistics of attitudes and unbiased length by sets are presented in Table 1.

The NW-SE set presents more vertical fractures. All attitudes measured in 3D (from DOM, field, and scanline) were plotted in a stereogram (Fig. 8). Most of the fractures are subvertical, with mean dips of: 73° (E-W), 75° (NE-SW e N-S), and 81° (NW-SE).

The 3D measurements (8A) are complementary to the 2D interpretation. The inclusion of different acquisition types aims to increase the number of measured fractures in an attempt to characterize all sets on different outcrop and digital outcrop scales, but it introduces sampling bias.

Field verification is also performed to verify interpretation (Fig. 8C) and kinematics. The point cloud measurements (Fig. 8B) highlight the E-W set, in the west portion of the site, and acquisition of the scanline adds fracture measurements to the NW-SE set (Fig. 8D) which is not as clear on the digital elevation model as it is in the field scale. Therefore, the combination of all 3D measurements reflect mostly the E-W and NW-SE sets.

The lengths were acquired in the 2D interpretation using DEM and in the 3D interpretation using DOM. The lengths of the segments range from a few meters to hundreds of meters, and when the fracture length is unbiased, they can reach kilometers (Fig. 9). NE-SW fractures have the longest maximum lengths, followed by E-W fractures, N-S and NW-SE show shorter fractures, while N-S fractures have higher censoring rates (EW: 11.3%, NE-SW: 12.0%, N-S: 12.5%, NW-SE:11.5%) due to interpretation boundaries and coverage of moraine deposits (Fig. 2C, D).

The best fit was a lognormal distribution, according to the rank proposed by Benedetti et al. (2024) since it reflects the actual measurements at the study site. The lognormal distribution is followed by the gamma, exponential, and power law distributions in the ranking.

A total fracture density (P21) of 0.051 [$m^{-}1$] was calculated for the entire fracture network. For each fracture set, we obtain fracture densities by set: 0.016 (E-W), 0.024 (NE-SW), 0.006 (N-S), 0.006 (NW-SE).

There are only a few measurements of aperture, and they are concentrated in one area where the scanline was acquired; for fractures that apparently are not very enlarged by dissolution (with maximum

Fig. 5. Example of fractures from each set: (A) N-S fault located in the central part of the study site, with vegetation development at the lower reliefs, (B) NE-SW faults and fractures developing a relay ramp between faults and dissolution along them, (C) E-W subvertical fractures with dissolution, (D) NW-SE persistent fracture corridor.

apertures of 0.400 cm), the values can then be considered as relative apertures. NE-SW and NW-SE fracture sets show similar mean apertures of approximately 0.400 cm, followed by the E-W set with a mean aperture of 0.275 cm, and N-S with a mean aperture of 0.162 cm.

3.2.2. Kinematics and geomechanics

Few normal displacements were recorded on the NE-SW, E-W, and N-S sets of faults, but strike-slip movement dominates throughout the fault population. The displacement is mostly dextral for the NE-SW striking faults, sinistral for the N-S set, dextral for the E-W, and sinistral for the NW-SE set, with local variations. The paleotensor analysis was performed from the structural features measured in the field (Fig. 10). Veins, tensile opened fractures, and stylolites were also considered to obtain the maximum stress tensor. When analyzing all sets together, we obtain a horizontal maximum stress in the NW-SE direction 120/02, when separating each set we obtain: for the NE-SW set a maximum stress in the WSW-ENE direction 82/13 (Fig. 10A), and for all the other sets E-W, N-S, and NW-SE a maximum stress in the NW-SE direction 148/01, 299/19, and 125/06, respectively (Figs. 10B, C, and D).

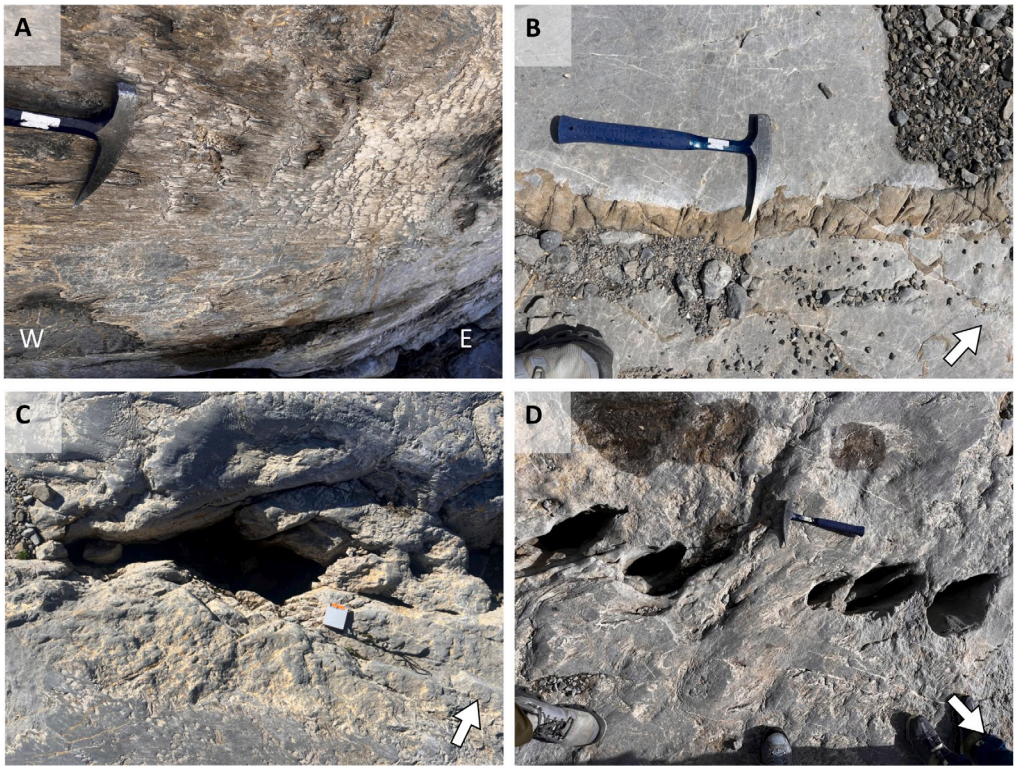

Fig. 6. Details of the structural and dissolution features: (A) slickenside indicating lateral movement (dextral), (B) NE-SW fracture filled with siderolitic deposits, (C) rhombohedric dissolution, (D) NW-SE fractures with en echelon dissolution.

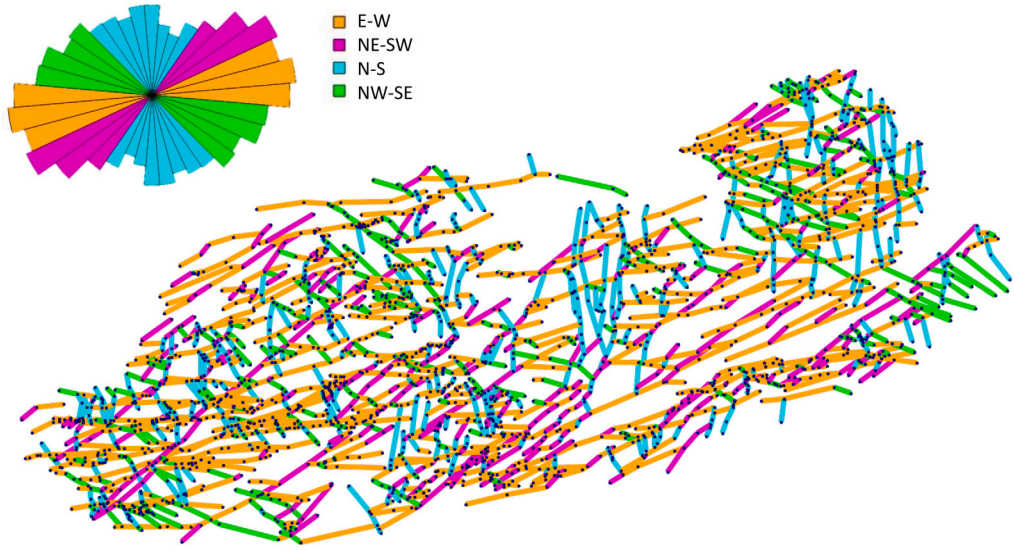

Fig. 7. Tsanfleuron fracture network as graphs colored by sets, the fracture intersections are the nodes (black dots) and the fracture branches are the edges (colored by set, E-W: orange, NE-SW: magenta, N-S: cyan, and NW-SE: lime). (For interpretation of the references to color in this figure legend, the reader is referred to the web version of this article.)

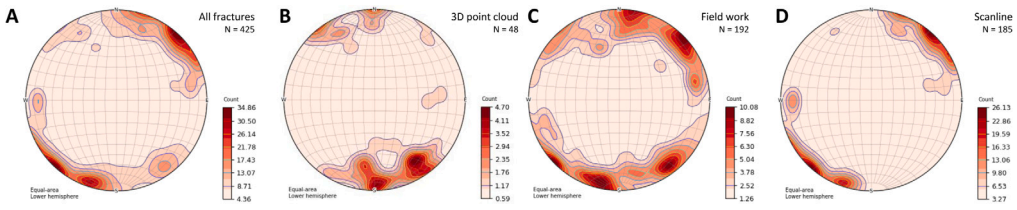

Fig. 8. Stereogram of fracture attitudes. (A) All 3D measurements. (B) From the 3D cloud point (DOM). (C) From field work. (D) From a scanline.

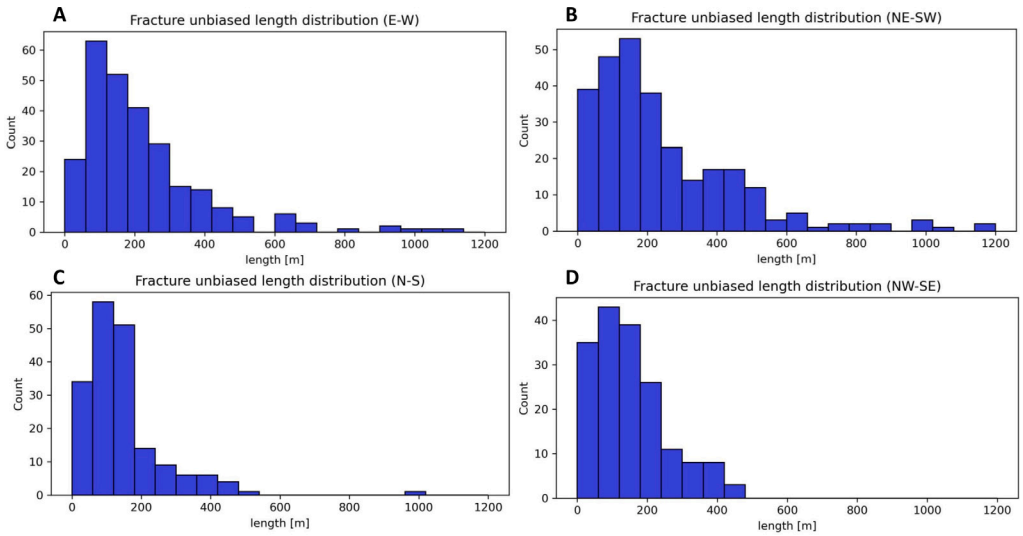

Fig. 9. Fracture length distribution considering censoring by fracture set. (A) E-W. (B) NE-SW. (C) N-S. (D) NW-SE.

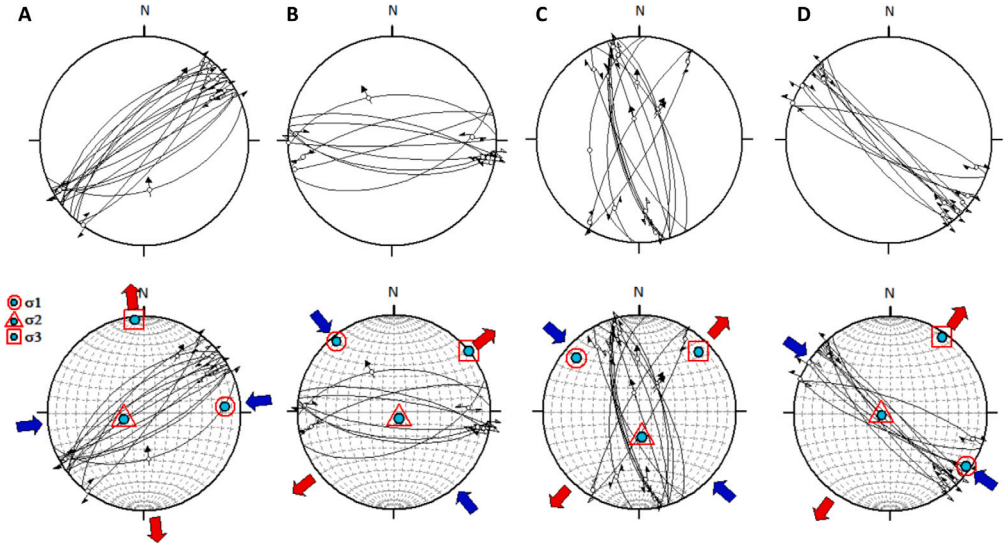

Fig. 10. Stereogram of faults (great circles) by set with slickensides (poles) and kinematics (arrows). The second row is the paleostress by set, with sigma 1 (circle), sigma 2 (triangle), and sigma 3 (square) obtained by inversion by set. (A) Set NE-SW. (B) Set E-W. (C) Set N-S. (D) Set NW-SE.

3.2.3. Degrees and age relationships

The degrees of the nodes are calculated to describe the topology (Fig. 11), the most recurrent fracture topologies of the simplified graph (Fig. 11A) are nodes of degree 1 that represent 51% of the data, nodes of degree 3 represent 34%, and nodes of degree 4 represent 14% of the total graph. Higher degrees are less frequent, representing less than 1% of the data. When we consider censoring (Fig. 11B), we obtain the following proportion of nodes: 57% (degree 1), 21% (degree 3), 15% (degree 4), and approximately 7% of the nodes censored.

To identify abutting and infer age relations between pairs of sets, we use directional topology. We count the number of degree 3 nodes and identify the sense of abutting (Table 2).

From the counting of the degree 3 nodes that abut each set, we compare the relationship between pairs and verify that E-W fractures abut all sets; NE-SW fractures abut N-S and NW-SE fractures; N-S fractures abut the NW-SE fractures. The result according to abutting, in order from older to younger, is: E-W, N-S, NE-SW, NW-SE. Combining counts from pairs of directions, we obtain higher interaction from sets E-W and NE-SW and lower interactions between the N-S and NW-SE sets.

Table 2
Quantification of abutting between pairs of family sets, the rows are the sets that abut (older) and the columns are the sets that are abutted (younger).

Abut \ Abutted	E-W	NE-SW	N-S	NW-SE
E-W	–	185	129	89
NE-SW	60	–	129	110
N-S	68	51	–	40
NW-SE	51	59	21	–

3.2.4. Centralities and percolation

Betweenness centrality was calculated to describe the connectivity of the network, highlighting the most important nodes in the fracture network, without any weight (Fig. 12A) and weighted by length (Fig. 12B).

The most important nodes follow an E-W and NE-SW path through the area, at the NE portion, they turn to an N-S path (Fig. 12A). When weighted by length, a similar but more continuous path is found (Fig. 12B). There is a minor NE-SW path in the SE portion of Tsanfleuron.

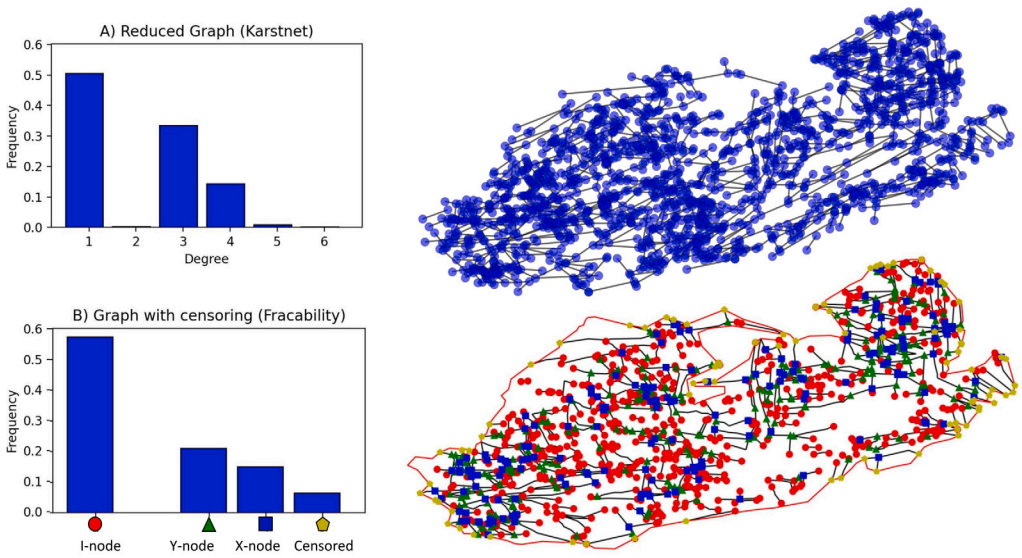

Fig. 11. Degree of the nodes from the fracture network. (A) Histogram and simplified graph generated in karstnet from the original graph. (B) Histogram and network generated in Fracability from GIS interpretation considering censoring.

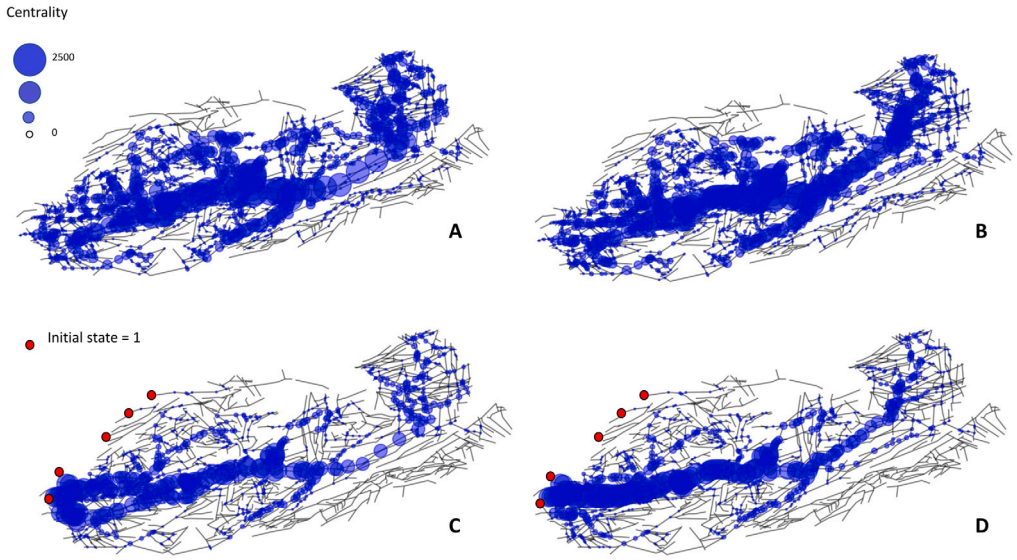

Fig. 12. Highlighting the importance of the nodes with the calculation of betweenness and percolation centrality for the fracture network of Tsanfleuron: (A) Betweenness centrality, (B) Betweenness centrality weighted by length, (C) Percolation centrality, and (D) Percolation centrality weighted by length.

The percolation centrality was calculated to describe the network connectivity that accounts for a dynamical state of the nodes, where we set an initial state of 1 for the nodes that are closer to the glacier, generating a better-defined E-W, ENE-WSW, and NE-SW path along the site (Fig. 12C). When weighted by length, the path becomes clearer and turns to NE-SW in the central portion, and N-S in the NE portion of Tsanfleuron (Fig. 12D). With changes in the nodes' state, it is possible to interpret the sense of the preferential flow path, that is, in general, eastward.

To evaluate how connected the network is and to have a measure of comparison to other fracture networks, we progressively removed nodes and verified the size of the connected components of the network. The network becomes largely fragmented when reaching a percolation threshold of about 20%–30% of node removal, suggesting moderate connectivity (Fig. 13).

4. Discussion

4.1. Geometry, age relationships, topology, and kinematics

The identification of four sets of fractures: E-W (85°), NE-SW (57°), N-S (176°), and NW-SE (117°) is in agreement with previous works by Gremaud (2008) and Gremaud et al. (2009) that defined four sets from older to younger as: E-W (90°), NE-SW (60°), N-S (0°), and NW-SE (135–145°), and Franck et al. (1984) that defined three fault and fracture systems, from older to younger: NE-SW (60–70°), N-S (180°), and NW-SE (130–150°), where the first correspond to a period before the formation of the Helvetic nappes, and NW-SE are still active (Franck et al., 1984). The dips are subvertical (Fig. 5B, C, D, and 8), with the NW-SE fracture set having a higher mean dip of 81°, which is consistent with the fact that the system is still active with a horizontal maximum stress in the same direction.

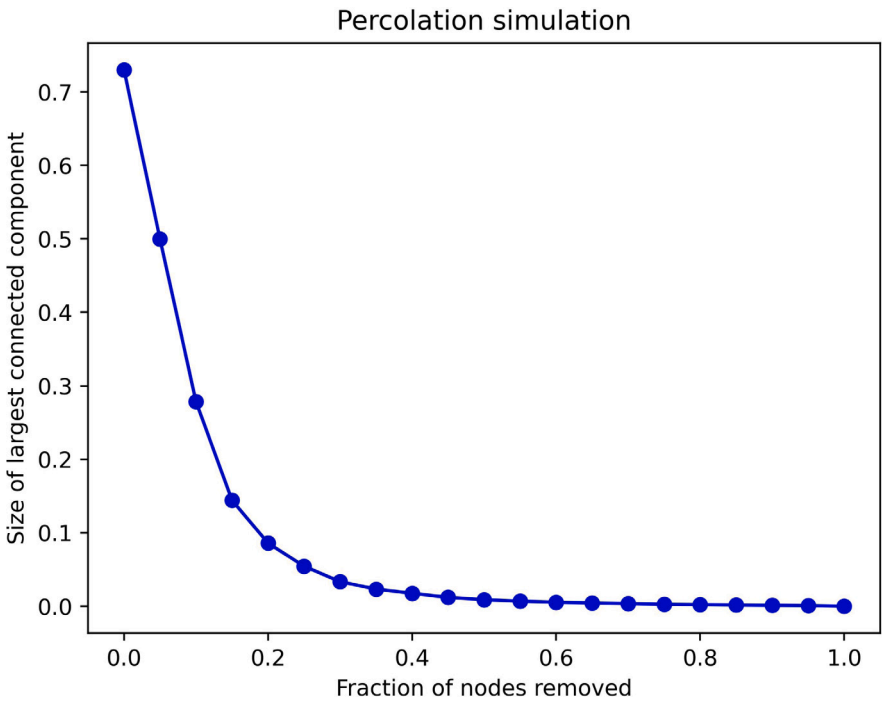

Fig. 13. Percolation simulation results for the Tsanfleuron fracture network as graphs.

The NE-SW system of faults and fractures is related to the fulfillment of siderolitic deposits at the end of the Cretaceous and beginning of the Tertiary (Franck et al., 1984; Epard, 2001; Gremaud, 2008; Gremaud et al., 2009). The N-S system corresponds to the main imbrication phase of the Helvetic nappes, and the NW-SE is related to the post-nappe phase and is still active, coinciding with an axis of maximum shortening deduced from the interpretation of earthquakes recorded by Franck et al. (1984) with a portable seismometer network. Gremaud (2008) and Gremaud et al. (2009) describe that the N-S set is not remarkable on a regional scale, but it is present on a local level, with extension apertures. The NE-SW is notable on all scales and is often filled with siderolitic deposits. The NW-SE fractures superpose the others and are more important in the western part of the study site, being more clearly identified in the field.

When we consider all different sources of data acquisition together, most of the fractures are oriented in the NE-SW ad E-W direction (Figs. 3, 7). However, when we consider the 3D measurements separately, we obtain a NW-SE trend (Fig. 8D) due to the sampling bias introduced with the NE-SW orientation of the scanline, designed to intersect the NW-SE fracture corridor and thus sample a greater number of orthogonal fractures. The sampling bias was introduced to better characterize the NW-SE set that was not as clear as the other sets in the DEM (Fig. 3).

From the abutting relationships between pairs of sets, we obtained age relationships similar to age relationships described by Franck et al. (1984), Gremaud (2008) and Gremaud et al. (2009). The E-W set is clearly the older set, presenting a higher number of nodes that abut all the other sets. The NE-SW set presents a higher number of abutting nodes towards the N-S set. The NW-SE set presents a lower number of nodes that abut the other sets, so it is abutted by all the other sets in the interpretation; therefore, it is the younger set. The total amount of abutting nodes in pairs of sets might indicate a higher interaction between sets E-W and NE-SW, and lower for sets N-S and NW-SE.

Set N-S is particularly clustered in the central part of Tsanfleuron, there is less space between the fractures in the N-S corridor and an underestimation of the intersections (Fig. 7) could occur. The geomorphology of the steps generated by the erosion of the N-S set of faults (Fig. 5A) also favors the underestimation of fractures in the central part of the site. The pattern of stairs indicates a relationship with the imbrication of the nappe. The N-S set is very localized between the exposure of the younger limestones (Eocene) towards the east and the older limestones (Cretaceous) towards the west, prominent where there is a lower relief, possibly related to folding. In agreement with what Franck et al. (1984) described as a direction related to the main imbrication phase of the Helvetic nappes.

When we consider censoring it is possible to have an unbiased fracture length (Fig. 9) and analyze the length distribution, even if they are covered by moraine deposits (Fig. 2D and Fig. 11B) or when they reach the boundary of the interpretations. This is especially important for the N-S fracture sets, as they are clustered at the central portion of the study site and are limited to the north by the moraine deposits. The lengths of the N-S fractures can reach kilometers in length. The NE-SW and E-W fractures are still longer in terms of length. The NW-SE sets present shorter lengths; they cut all the other sets, but are more discontinuous in terms of length.

Other than the censoring effect, fracture length is also biased by the resolution effects, called truncation (Bonnet et al., 2001), as the frequencies of smaller lengths are underestimated due to the nature of the acquisition and measurements that are limited to the scale of fracture interpretation and to the pixel resolution of the digital models.

A relative areal fracture intensity (P21) reinforces what we describe for the interpretation of fractures using the DEM, that NE-SW fractures are longer, more frequent, and concentrated than the E-W fractures, followed by less frequent N-S and NW-SE fractures.

We analyze the kinematics of all sets together previously from the set definition, obtaining a directed maximum compression in the NW-SE direction, in agreement with the maximum horizontal compressive stress found in previous work (Pavoni, 1980; Franck et al., 1984) and registered for the region (Heidbach et al., 2016).

For the generalization of the kinematics by set, we obtain mostly dextral displacement for the E-W and NE-SW sets, sinistral displacement for the N-S set, and for the NW-SE mostly sinistral. If we consider the age relationships described by Franck et al. (1984), Gremaud (2008) and Gremaud et al. (2009), we can analyze each set separately, but we account mainly for records of strike-slip movements.

As the filling of siderolitic deposits, in some of the NE-SW structures (Fig. 5F) defines them as one of the older sets, the high degree of dissolution also indicates more exposition over time. We analyzed the NE-SW set separately from the others. The paleostress inversion for the NE-SW set alone resulted in a maximum horizontal stress in the WSW-ENE direction, and all the other sets analyzed separately resulted in a NW-SE maximum horizontal stress.

4.2. Connectivity, fluid flow, and hydrogeology

Connectivity analysis is performed for the whole network considering the two aspects of it, such as the importance of interconnected nodes, in terms of degrees and centralities, and the definition of a threshold for connectivity, in terms of percolation (Sanderson and Nixon, 2018).

The graph-based fracture modeling approach can combine the important factors that influence connectivity: orientation, length, density, and topology in one graph, being scale independent as topology measures are dimensionless (Sanderson and Nixon, 2018). This approach will represent coherent connectivity related to the selected interpretation scale, although the interpretation scale still matters for the representation of the desired fracture sets.

From the fracture networks as graphs we calculate the importance of each node; therefore, we get some insights about preferential fluid flow previously from modeling and flow simulation. To identify the most important nodes in the network, we calculate the degrees and centralities, nodes that have a higher degree, and higher centralities are the most important intersections of the fracture network.

As described by Sanderson et al. (2019) and Manzocchi (2002) most of the nodes in the fracture networks have lower degrees 1, degrees 3 represent abutting, and degrees 4 represent cross-cutting. The degree calculation and the identification of the nodes of the Tsanfleuron fracture network show that lower degree topologies occur more often and degrees higher than 4 are rare, because radial patterns, or star shape, can be more related to impact structures than to the tectonic stresses. Nodes that have a higher degree are more connected to other nodes, in Tsanfleuron, they are more concentrated in the SW limit, then in the central *N* part of the area, and in the NE portion.

Betweenness centrality highlights the importance of the nodes as they are serving as connectors to a greater number of shortest paths (12A, B). The most important nodes connect a E-W and NE-SW preferential pathways, with a local variation on the NE part of the study area, where there are nodes with a higher degree and betweenness centrality following an N-S direction. When we apply a weight by length, the pattern is similar, but the paths are more continuous.

The percolation centrality also gives hints about the sense of the connection, as we attribute higher initial states for the nodes close to the glacier (12B,C). The pattern is similar to the result from betweenness centrality, but it is more continuous and gives the sense of change in the initial state eastward. The percolation centrality is equal to the betweenness centrality when the initial states are the same for all nodes, if recharge is coming from the rain we can evaluate the scenarios with betweenness centrality and the pathways are more spread throughout the study site, whereas if the recharge is coming from the front of the glacier, we can evaluate preferential paths with percolation centrality and the paths are more continuous eastward. We highlight that this type of evaluation requires a more detailed evaluation with additional consideration of the karst features and bedding.

Topology and percolation are important to compare connectivity in different systems and are key issues for future fracture modeling and simulation, as we expect to achieve more realistic conductivities by maintaining coherent topologies in a simulation using a graph-based approach, as the connectivity of stochastic models like the discrete fracture network (DFN) models "can be very different from natural networks" (Sanderson and Nixon, 2018).

Connectivity is evaluated to describe today's preferential fluid flow paths, but can also be thought of as previous dissolution pathways for karst development. Taking into account that the limestone aquifer is above a marl layer, the gentle dip of the bedding towards ENE, E, and ESE, and the connection of the most important nodes, we infer the dissolution path towards NE, ENE, and E in limestone preferentially through the fractures (Tanaka et al., 2025).

NE-SW fractures are enlarged by dissolution with the development of a paleokarst previously from the deposition of the siderolitic Eocene deposits. The N-S fractures also show a high development of dissolution, with a stair step erosion (Fig. 5A). NW-SE fractures often show a dissolution in en echelon pattern (Fig. 6D) and sometimes register the first stages of a more recent conduit development. Even when there is no karst development, the NW-SE structures have apertures comparable to the apertures of the NE-SW set (Fig. 5D). All sets show a development of dissolution, but larger conduits developed mainly in the NE-SW, ENE-WSW, and E-W directions (Tanaka et al., 2025). We interpret that most of the fractures are open due to dissolution, and in a geomechanical perspective, we verify that the NW-SE fractures are open, as they are aligned with the actual maximum horizontal compression.

According to Gremaud et al. (2009) groundwater circulation occurs mainly near the base of the shallow fractured and karstified Urgonian limestone, the most important aquifer in the area, because it is underlaid by marls that are described as a regional aquiclude (Gremaud et al., 2009). Therefore, analyzing today's preferential fluid flow paths, in a hydrogeological point of view, we can infer water flow in the exposed pavement towards NE, ENE, and E. We use the same logic that was used before, that fractures play a major role for fluid flow, the gentle dip of the bedding, and that the main aquifer is underlaid by marls, and we add the fact that all fractures can be considered opened, presenting high dissolution degrees.

It is a challenge to extend the interpretation beyond the limits of the pavement, for example, in the SE portion of Tsanfleuron, between Col de Sanetsch and Glarey spring (Fig. 2), where the fractures are covered by vegetation and debris flow deposits, making it difficult to interpret the fracture pattern.

The shoulder in the SE portion of the study site presents greater relief, as a result of the imbrication of the Diablerets and Mont Gond nappes, it generates a type of wall limited by two parallel NE-SW faults (Fig. 2D, E) with a higher inclination of the pavement towards SE, which also makes the interpretation of the preferential flow path harder. By extending the interpretation of the NW-SE fractures from the closest portion of the pavement, we are able to infer preferential paths in the same direction, aided by the slope of the higher relief shoulder. A change in flow northeastward, before the shoulder, to southeastward after the shoulder can be interpreted for the SE portion of Tsanfleuron beyond the pavement. This flexion can also be due to the geometry of the front of the Diablerets nappe (Fig. 2), as its front is folded, making higher dips at the border and working as an accumulation of fluids in the folded strata of the limestone, for example, in the direction of the Glarey spring.

5. Conclusion

Graph-based analysis of fracture networks allows the combination of various aspects of structural geology in one graph, adding new data, interpretation, and topology characterization to the study site framework, providing insights into fracture characterization and identification of fluid flow paths in the Western Swiss Alps. The application of graph tools to fracture modeling can simplify the representation of fracture networks while preserving their inherent complexity, and open new perspectives for the calculation of nodes importance, characterizing coherent conductivities. This approach is suitable for different scales as it takes into account the topology of the network, and does not require

a grid/mesh in the early stages of fracture network characterization and geomodeling.

The interpretation of fractures in the DEM is the input to build the graph and calculate geometrical and topological parameters. The interpretation of the fracture attitude in the virtual outcrops matches the measurements made in the field and is especially important for inaccessible areas.

Four main sets of subvertical fractures were identified according to azimuths, in chronological order: E-W (85°), NE-SW (57°), N-S (176°), and NW-SE (117°). We identified in general dextral displacement for the E-W and NE-SW sets, sinistral displacement for the N-S set, and for the NW-SE set with local variations. All fracture sets are generally open by dissolution, especially the still active NW-SE set, which is also open by the NW-SE horizontal maximum stress. NE-SW fractures are longer than the others and present higher dissolution with the development of conduits, together with the E-W set.

Betweenness and percolation centralities highlight the connection of the most important nodes in NE-SW, ENE-WSW, and E-W directions. The network is moderately connected, with a percolation threshold of about 20 to 30%. The gentle dip of the bedding, the underlying marls, and the subvertical nature of the fractures allow the interpretation of preferential flow pathways from the 2D fracture network characterization and the graph-based analysis towards NE, ENE, and E on the pavement.

By extending the interpretation of the NW-SE fractures towards SE we can infer preferential paths in the NW-SE direction, aided by the slope of the higher relief of the shoulder of the Diablerets nappe, towards the Glarey Spring. A change in direction can be due to the geometry of the front of the Diablerets nappe (Fig. 2B,D,E), as its front is folded, which facilitates the accumulation of fluids in the folded strata of the limestone.

The next step following the characterization of the fracture network will be a quantitative analysis of the links between fracture and karst, which can be used for future work of the karst network and the hydrogeological modeling of Tsanfleuron. The proposed methodology and tools can be extended to other study sites and various applications.

CRediT authorship contribution statement

Ana Paula Burgoa Tanaka: Writing – review & editing, Writing – original draft, Visualization, Validation, Software, Methodology, Investigation, Formal analysis, Data curation, Conceptualization. **Philippe Renard:** Writing – review & editing, Validation, Supervision, Methodology, Conceptualization. **Jefter Natan de Moraes Caldeira:** Writing – review & editing, Validation, Investigation, Formal analysis, Conceptualization. **Celia Trunz:** Writing – review & editing, Software, Investigation, Data curation, Conceptualization.

Declaration of competing interest

The authors declare the following financial interests/personal relationships which may be considered as potential competing interests: Ana Paula Burgoa Tanaka reports a relationship with Petrobras that includes: employment. If there are other authors, they declare that they have no known competing financial interests or personal relationships that could have appeared to influence the work reported in this paper.

Acknowledgments

The authors acknowledge Xiao Xia Liang and Julien Straubhaar for their contribution to the initial development of this work. Special thanks to Manon Trottet for discussions about the study site. We also thank Robin Voland, Alex Kobayashi, Tanguy Racine, Nina Egli, Anindita Samsu, Margot Dupuis, and Arnaud de Prarochet.

References

Aharony, A., Stauffer, D., 2003. Introduction To Percolation Theory. Taylor & Francis.
Andresen, C.A., Hansen, A., Le Goc, R., Davy, P., Hope, S.M., 2013. Topology of fracture networks. Front. Phys. 1, 7.
Badoux, H., Bonnard, É.G., Burri, M., 1959. St-Léonard: Avec Annexe De La Feuille Sion, Topographie: Carte Nationale 1: 50 000, Feuille Normale Montana-W.... Schweizerische Geologische Komm..
Benedetti, G., Casiraghi, S., Bertacchi, D., Bistacchi, A.L.P., 2024. Unbiased statistical length analysis of linear features: Adapting survival analysis to geological applications. EGUsphere 2024, 1–34.
Bonnet, E., Bour, O., Odling, N.E., Davy, P., Main, I., Cowie, P., Berkowitz, B., 2001. Scaling of fracture systems in geological media. Rev. Geophys. 39 (3), 347–383.
Brandes, U., 2008. On variants of shortest-path betweenness centrality and their generic computation. Soc. Netw 30 (2), 136–145.
Casiraghi, S., Benedetti, G., Bertacchi, D., Mittempergher, S., Agliardi, F., Monopoli, B., La Valle, F., Martinelli, M., Bigoni, F., Albertini, C., Bistacchi, A., 2025. Quantitative parametrization of fracture networks in digital Outcrop models: an optimized workflow. EGUsphere 2025, 1–55.
Collon, P., Bernasconi, D., Vuilleumier, C., Renard, P., 2017. Statistical metrics for the characterization of karst network geometry and topology. Geomorphology 283, 122–142.
Delvaux, D., Sperner, B., 2003. New aspects of tectonic stress inversion with reference to the TENSOR program. Geol. Soc. Lond. Spec. Publ. 212 (1), 75–100.
Dershowitz, W., Herda, H.H., 1992. Interpretation of fracture spacing and intensity. 33rd U.S. Symp. Rock Mech. USRMS 1992 All Days ARMA–92–0757.
Epard, J.l., 2001. The overall tectonic framework of the externides domain. In: Borel, G., Bussy, F., Capuzzo, N., Epard, J., Escher, A., Marchant, R., Marthaler, M., Mosar, J. (Eds.), Geology of the western Swiss Alps, A Guide Book. In: Mémoires de Géologie (Lausanne), vol. 36, pp. 43–51.
Escher, A., Masson, H., Steck, A., 1993. Nappe geometry in the western Swiss Alps. J. Struct. Geol. 15 (3–5), 501–509.
Franck, P., Wagner, J.J., Escher, A., Pavoni, N., 1984. Évolution des contraintes téctoniques et sismicité dans la région du col du Sanetsch, Alpes valaisannes helvétiques. Eclogae Geol. Helv. 77 (2), 383–393.
Freeman, L.C., 1977. A set of measures of centrality based on betweenness. Sociometry 40 (1), 35–41.
Gremaud, V., 2008. Géologie du karst de tsanfleuron. Collect. EDYTEM. Cah. Géographie 7 (1), 127–134.
Gremaud, V., Goldscheider, N., Savoy, L., Favre, G., Masson, H., 2009. Geological structure, recharge processes and underground drainage of a glacierised karst aquifer system, Tsanfleuron-Sanetsch, Swiss Alps. Hydrogeol. J. 17 (8), 1833–1848.
Grohmann, C.H., Campanha, G., 2010. OpenStereo: open source, cross-platform software for structural geology analysis. In: AGU Fall Meeting Abstracts, vol. 2010, pp. IN31C–06.
Hagberg, A., Swart, P., S. Chult, D., 2008. Exploring Network Structure, Dynamics, and Function Using Networkx. Technical Report, Los Alamos National Lab.(LANL), Los Alamos, NM (United States.
Heidbach, O., Rajabi, M., Reiter, K., Ziegler, M., 2016. World Stress Map Database Release 2016. V. 1.1.. Technical Report, GFZ Data Services.
Manzocchi, T., 2002. The connectivity of two-dimensional networks of spatially correlated fractures. Water Resour. Res. 38 (9), 1–1–1–20.
Neven, A., Dall'Alba, V., Juda, P., Straubhaar, J., Renard, P., 2021. Ice volume and basal topography estimation using geostatistical methods and ground-penetrating radar measurements: application to the Tsanfleuron and Scex Rouge glaciers, Swiss Alps. Cryosphere 15 (11), 5169–5186.
Nyberg, B., Nixon, C.W., Sanderson, D.J., 2018. NetworkGT: A GIS tool for geometric and topological analysis of two-dimensional fracture networks. Geosphere 14 (4), 1618–1634.
Pavoni, N., 1980. Crustal stresses inferred from fault-plane solutions of earthquakes and neotectonic deformation in Switzerland. In: Scheidegger, A.E. (Ed.), Tectonic Stresses in the Alpine-Mediterranean Region. Springer Vienna, Vienna, pp. 63–68.
Peacock, D.C., Nixon, C.W., Rotevatn, A., Sanderson, D.J., Zuluaga, L., 2016. Glossary of fault and other fracture networks. J. Struct. Geol. 92, 12–29.
Peacock, D., Sanderson, D., 2018. Structural analyses and fracture network characterisation: Seven pillars of wisdom. Earth-Sci. Rev. 184, 13–28.
Piraveenan, M., Prokopenko, M., Hossain, L., 2013. Percolation centrality: Quantifying graph-theoretic impact of nodes during percolation in networks. PLOS ONE 8 (1), 1–14.
Rizzo, R.E., Healy, D., De Siena, L., 2017. Benefits of maximum likelihood estimators for fracture attribute analysis: Implications for permeability and up-scaling. J. Struct. Geol. 95, 17–31.
Sævik, P., Nixon, C., 2017. Inclusion of topological measurements into analytic estimates of effective permeability in fractured media. Water Resour. Res. 53 (11), 9424–9443.
Sanderson, D.J., Nixon, C.W., 2015. The use of topology in fracture network characterization. J. Struct. Geol. 72, 55–66.
Sanderson, D.J., Nixon, C.W., 2018. Topology, connectivity and percolation in fracture networks. J. Struct. Geol. 115, 167–177.

Sanderson, D.J., Peacock, D.C., 2020. Making rose diagrams fit-for-purpose. Earth-Sci. Rev. 201, 103055.
Sanderson, D.J., Peacock, D.C., Nixon, C.W., 2024. Fracture sets and sequencing. Earth-Sci. Rev. 257, 104888.
Sanderson, D.J., Peacock, D.C., Nixon, C.W., Rotevatn, A., 2019. Graph theory and the analysis of fracture networks. J. Struct. Geol. 125, 155–165.
Santiago, E., Velasco-Hernández, J.X., Romero-Salcedo, M., 2016. A descriptive study of fracture networks in rocks using complex network metrics. Comput. Geosci. 88, 97–114.
Schoeneich, P., Reynard, E., 2021. Structural landscapes and relative landforms of the diablerets massif. In: Landscapes and Landforms of Switzerland. Springer International Publishing, pp. 123–141.
Steck, A., Epard, J., Escher, A., Gouffon, Y., Masson, H., 2001. Carte tectonique des alpes de suisse occidentale. Not. Explic. Landeshydrol. Und–Geologie Bern.
Steck, A., Epard, J.L., Escher, A., Lehner, P., Marchant, R., Masson, H., 1997. Geological interpretation of the seismic profiles through Western Switzerland: Rawil (W1), Val d'Anniviers (W2), Mattertal (W3), Zmutt-Zermatt-Findelen (W4) and Val de Bagnes (W5).. Deep. Struct. Swiss Alps-Results from NRP 20 123–137.
Tanaka, A.P.B., 2025. Anapaulabtanaka/tsanfleuron_fracture_networks: v1.1. http://dx.doi.org/10.5281/zenodo.15739431.
Tanaka, A.P.B., Trunz, C., Trottet, M., Racine, T., Renard, P., 2025. Detecting fracture networks and karst features alignments similarities in the aquifer system of Tsanfleuron, Swiss Alps. In: EGU General Assembly 2025, vol. 2025, p. 11154.
Thiele, S.T., Jessell, M.W., Lindsay, M., Ogarko, V., Wellmann, J.F., Pakyuz-Charrier, E., 2016. The topology of geology 1: Topological analysis. J. Struct. Geol. 91, 27–38.
Valentini, L., Perugini, D., Poli, G., 2007. The "small-world" topology of rock fracture networks. Phys. A 377 (1), 323–328.